# Turbulence and scalar flux modelling applied to separated flows

by

Johan Gullman-Strand

December 2004 Doctoral Thesis from Royal Institute of Technology Department of Mechanics SE-100 44 Stockholm, Sweden

## CHAPTER 1

# Introduction

The curiosity to investigate and need to describe the world surrounding us are key elements of human nature. Despite the continuous advancements in science and technology, there are still some areas that will never be fully understood or satisfactory described. Fluid mechanics, in general, or more popularly named aerodynamics, and more specific turbulent flow is one of these areas.

As you step outside and feel the breeze hit your face, you experience a turbulent flow that surrounds us. The leaves falling from the trees have complicated vortical structures in the turbulent wake forming on the upper side, forcing them into the characteristic dance towards the earth. Even in your office, you can hear the noise from the ventilation and the cooling fans of the computers. These noises are, to some extent, generated by the chaotic motion of the air.

The exact equations describing fluid flow, the Navier-Stokes equations of momentum and continuity, have been known for a very long time. The difference in sizes of the vortices, or rather the ranges of spatial and temporal scales, in a turbulent flow are so great that it is only possible to compute or simulate all details of the motion of a fluid for a restricted class of flows, such as boundary layers, wakes and jets. The main restriction is the ratio of inertial forces to viscous forces in the fluid, called Reynolds number. For low Reynolds numbers the viscous forces maintain an ordered flow which follows well-ordered streamlines. As the inertial forces increase, the stability of these streamlines deteriorates and the motion of a fluid particle becomes chaotic. Here, it is meaningful to introduce the concept of scales to the flow. In such a flow, that we refer to as turbulent, we can observe a range of scales (or eddy sizes). This range increases with increasing Reynolds number. A characteristic feature is the energy flux from large to smaller scales through the cascade process. This breakdown of large eddies to subsequently smaller ones also means that the small scales have a universal character with a high degree of independence of initial conditions and geometrical restrictions of the global flow.

Even though fluid flow is governed by a specific set of equations, the characteristics of the turbulent motion are not uniquely defined. According to Tennekes & Lumley (1972), the nature of turbulence can be characterized by the following:

## 2 1. INTRODUCTION

- Turbulent flow is *irregular* and one has to rely on statistical methods to describe the behavior.
- High levels of *fluctuating vorticity* in three dimensions giving rise to the vortex stretching mechanism.
- Turbulence is a feature of a flow of a *continuum*. The smallest length scales are far greater than the molecular counterparts.
- The instabilities in a turbulent flow occur at high Reynolds numbers.
- To be turbulent, the flow has to exhibit diffusive effects which causes rapid mixing and increased rates of e.g. heat transfer.
- Without a continuous feed of energy, the turbulence rapidly dies out. This is due to the *dissipative* nature of the flow.

The effort to accurately calculate fluid flows relies on the computations of the system of governing partial differential equations (PDE).

For engineering flow predictions, the mean flow field is obtained through solution of the Reynolds averaged Navier-Stokes equations. These equations contain the Reynolds stress tensor that has to be described through turbulence modeling. The aim of this type of modeling is to construct a closed set of differential and algebraic relations from which the Reynolds stress tensor, and thereby the mean flow, can be determined.

The complexity of the complete set of model equations for the mean flow and turbulence quantities can be considerable, depending on the choice of level in the hierarchy of single-point models, since they are based solely on statistical moments evaluated at a single point. Several books and review papers on this topic have appeared recently (Piquet (1999), Johansson (2002)) although the first steps in this field were taken more than a century ago. The development of models for actual computational fluid dynamics (CFD) calculations can be said to have been established in the 1970's. Since then, a variety of different types of models have been developed, including models for compressible flow, passive and reactive scalars etc.

A general trend in turbulence modeling has been to aim for a higher degree of generality than in earlier models. For instance, the satisfaction of physical realizability constraints can significantly reduce the need for ad-hoc damping functions in the vicinity of solid walls. The price to pay is often a higher degree of complexity of the models.

The applications of CFD in industry ranges from internal flows, e.g. in ventilation systems, computer housings and engine air intakes, to external flows, mostly associated with aerospace applications like airfoil or aircraft aerodynamics but also wind-energy power-plants and automotive (cars and trucks) design. The demands on lower fuel consumption for new cars can be achieved in part by reducing the aerodynamic drag. The aerodynamic noise generated at high speeds on the Shinkansen and TGV trains in Japan and France is classified as noise-pollution and must be improved in order to reduce the impact on the surroundings.

The framework of equations governing fluid flow can be expanded to include the transport of passive scalars. The definition of a passive scalar is a quantity that is affected by the flow without itself affecting the flow. Typical examples of approximations of passive scalars in air are temperature, moisture concentration of pollution particles. This approximations have some restrictions since buoyancy effects may enter when heat, or temperature is involved, and the pollution particles must be small enough not to be affected by gravity.

The development, testing and validation of turbulence models can be very time consuming. Thanks to the concept of automated code generation, the time spent on this process can be reduced significantly. By defining the model in a clear readable format at the highest possible level, effort can be spent on the formulation of equations instead of numerical implementation and the risk of human introducing human errors is thereby reduced.

# CHAPTER 2

# Governing equations

Fluid flow is governed by the Navier-Stokes equations for momentum and continuity. In tensor formulation for an incompressible fluid they read

$$\frac{\partial \tilde{u}_i}{\partial t} + \tilde{u}_j \frac{\partial \tilde{u}_i}{\partial x_j} = -\frac{1}{\rho} \frac{\partial \tilde{p}}{\partial x_i} + \frac{\partial}{\partial x_j} (2\nu \tilde{s}_{ij})$$
 (2.1)

$$\frac{\partial \tilde{u}_i}{\partial x_i} = 0 \tag{2.2}$$

with  $\tilde{u}_i$  and  $\tilde{p}$  as the instantaneous velocity components and pressure field. The constants for density and kinematic viscosity are denoted  $\rho$  and  $\nu$ ,  $\tilde{s}_{ij} \equiv \frac{1}{2}(\tilde{u}_{i,j} + \tilde{u}_{j,i})$  is the instantaneous strain rate tensor. This set of equations governs turbulent flow ranging from the smallest scales of space and time, the Kolmogorov scales, to the scales of the geometry to be computed. The size of the smallest eddies decrease as the Reynolds number increased. The whole range of scales is taken into account in Direct Numerical Simulations (DNS). This approach in today feasible only for a few simple geometries and for low to moderate Reynolds numbers. In the statistical approach to flow prediction we introduce a split of the instantaneous quantity into an average and a fluctuating part. In the case of the Navier-Stokes equations  $\tilde{u}_i = U_i + u_i$  and  $\tilde{p} = P + p$ . By inserting this decomposition and taking the ensemble average the Reynolds Averaged Navier-Stokes (RANS) equations for the mean velocity field are obtained

$$\frac{\mathrm{D}U_i}{\mathrm{D}t} = -\frac{1}{\rho} \frac{\partial P}{\partial x_i} + \frac{\partial}{\partial x_j} (2\nu S_{ij} - \overline{u_i u_j}) \tag{2.3}$$

$$\frac{\partial U_i}{\partial x_i} = 0 \tag{2.4}$$

where  $\overline{u_i} = \overline{p} = 0$  and the mean strain rate is defined as  $S_{ij} = \frac{1}{2}(U_{i,j} + U_{j,i})$ . The last term in equation (2.3),  $-\overline{u_iu_j}$ , is the single-point velocity fluctuation correlation which is the source of turbulence modelling in computational fluid dynamics (CFD). We refer to  $-\rho \overline{u_iu_j}$  as the Reynolds stress tensor. In equation (2.3), D/Dt is not the exact material derivative, instead it denoted the derivative following the mean flow, hence D/Dt =  $\partial/\partial t + U_j(\partial/\partial x_j)$ .

## 2.1. Reynolds Stress Models

There are several levels of modelling to consider when solving for the Reynolds stress tensor. From the complex second order closures in differential Reynolds stress model (DRSM) where six transport equations for  $\overline{u_i u_j}$  have to be solved for 3D (four equations in 2D), down to relatively simple eddy-viscosity models with a linear relation for the Reynolds stresses in mean strain rate  $S_{ij}$ . If instead the Reynolds stress anisotropy tensor  $a_{ij}$  is used, where

$$a_{ij} = \frac{\overline{u_i u_j}}{K} - \frac{2}{3} \delta_{ij} \tag{2.5}$$

and K denote the kinetic energy of the turbulent eddies,  $K = \frac{1}{2}\overline{u_iu_i}$ , an algebraic expression (ARSM) can be obtained. With an appropriate choice of model parameters, an explicit algebraic model (EARSM) is reached where  $a_{ij}$  is a function of the mean strain and rotation rate tensors,  $S_{ij}$  and  $\Omega_{ij}$ . The most straightforward approach is to use the Boussinesq hypothesis, or eddy-viscosity assumption, and introduce an eddy viscosity  $\nu_T$ , which in contrast to the molecular viscosity  $\nu$  is a property of the flow rather than of the fluid.

The RSM usually need additional equations to close the system of equations. This is most commonly handled by transport equations for the velocity and lengthscale determining quantities. The velocity scale is solved implicitly in DRSM, thus only one lengthscale determining equation is needed. For EARSM and eddy viscosity models a two-equation system based on the turbulence kinetic energy for the velocity scale and some other quantity, such as  $\varepsilon$ , denoting the dissipation rate of K.

Near-wall correction terms can be introduced at any level of modelling to better describe the large gradients in most quantities close to solid wall. This is commonly called low-Reynolds number corrections and based on a local Reynolds number formulated to decrease in the proximity of walls. Different versions of low-Re models for DRSM, EARSM and two-equation turbulence models are presented in sections 2.1.2, 2.1.5 and 2.2.1.

## 2.1.1. Differential Reynolds stress model

A differential transport equation for the fluctuating velocity field can be derived in the same way as the RANS equations (2.3), expressed as

$$\frac{D\overline{u_i u_j}}{Dt} = \mathcal{P}_{ij} + \varepsilon_{ij} + \Pi_{ij} + \frac{\partial}{\partial x_k} \left( \nu \frac{\partial \overline{u_i u_j}}{\partial x_k} - J_{ijk} \right)$$
 (2.6)

with the terms on the right hand side corresponding to production, dissipation, pressure-strain rate correlation, viscous diffusion and spatial redistribution due to inhomogeneities. Both the production term and the viscous diffusion are defined in known quantities, while the other three terms need to be approximated. E.g. the spatial redistribution tensor  $J_{ijk}$ , which contains the triple velocity correlation  $\overline{u_iu_ju_k}$ . The production tensor is uniquely defined as

$$\mathcal{P}_{ij} = -\overline{u_i u_k} U_{j,k} - \overline{u_j u_k} U_{i,k} \tag{2.7}$$

where  $U_{i,j}$  is the mean velocity gradient tensor. A lot of efforts have been put into the modelling of  $\varepsilon_{ij}$  and  $\Pi_{ij}$ . Without going into too many details of modelling of the pressure-strain rate correlation, we can state that it may be lumped together with the dissipation rate anisotropy  $e_{ij} = \varepsilon_{ij}/\varepsilon - \frac{2}{3}\delta_{ij}$ . A general expression for the combined term that is linear in the Reynolds stress tensor is

$$\frac{\mathbf{\Pi}}{\varepsilon} - \mathbf{e} = -\frac{1}{2} \left( C_1^0 + C_1^1 \frac{\mathcal{P}}{\varepsilon} \right) \mathbf{a} + C_2 \mathbf{S} 
+ \frac{C_3}{2} \left( \mathbf{a} \mathbf{S} + \mathbf{S} \mathbf{a} - \frac{2}{3} \operatorname{tr} \{ \mathbf{a} \mathbf{S} \} \mathbf{I} \right) - \frac{C_4}{2} \left( \mathbf{a} \mathbf{\Omega} - \mathbf{\Omega} \mathbf{a} \right)$$
(2.8)

where  $C_1^0$ – $C_4$  are model dependent. Most linear models may be written in this form. Bold face matrix notation is introduced in (2.8) for brevity, where e.g. **aS** denotes the inner product  $a_{ik}S_{kj}$ . In the model of Launder et al. (1975) (LRR), the dissipation rate tensor was assumed to be isotropic  $(e_{ij} = 0)$  and the pressure-strain rate tensor was split int a slow and rapid part. The Rotta model was adopted for the slow part with the constant  $c_1$  while the constant  $c_2$  controlled the rapid part, see details in Paper 3. The values for  $c_1$  and  $c_2$ originally proposed in the LRR model were 1.5 and 0.4 respectively but later increased to 1.8 and 5/9 by Wallin & Johansson (2000). The original LRR model also contained a wall-reflection term for obtaining the correct behavior in boundary layers. However, the wall-reflection term is not needed with the recalibrated  $c_1$  and  $c_2$  and is, thus, not further considered in this study. In Paper 3 the value of  $c_2 = 0.6$  was used to compare with an attempt to lower the effective turbulence viscosity in an ERASM framework. The model with the higher (modified) values is here denoted mod-LRR. A non-linear model was proposed by Speziale et al. (1991) (SSG), linearized around equilibrium homogenous shear flow by Gatski & Speziale (1993) (lin-SSG). Later Craft & Launder (1996) proposed a low-Re model including expressions also for the dissipation and redistribution tensors.

The exact expression for the spatial redistribution term contains a triple velocity correlation  $\overline{u_i u_j u_k}$  as well as pressure-velocity correlations,

$$J_{ijk} = -\overline{u_i u_j u_k} - \frac{1}{\rho} \left( \overline{p u_j} \delta_{ik} + \overline{p u_i} \delta_{jk} \right). \tag{2.9}$$

This shows one of the closure problems with this level of turbulence modelling. Launder  $et\ al.$  assumed that the pressure fluctuations could be neglected and modelled the remaining the triple velocity correlation. Daly & Harlow (1970) proposed a turbulent diffusion term formulated for an arbitrary scalar, here adopted to the  $\overline{u_iu_j}$ -tensor as

$$\mathcal{D}_{ij}^{t} = \frac{\partial}{\partial x_{k}} \left( c_{s} \frac{K}{\varepsilon} \overline{u_{k} u_{l}} \frac{\partial \overline{u_{i} u_{j}}}{\partial x_{l}} \right)$$
 (2.10)

with  $c_s$  as a model parameter.

All of the above described models include the modelling of a length scale determining quantity, here symbolised by  $\varepsilon$ . Paper 3 shows how an expression for the inverse turbulence time-scale can be used instead, including re-calibration of diffusion parameters  $c_s$  and  $c_{\omega}$ .

## 2.1.2. Low-Reynolds number DRSM

The original LRR model is not valid through the viscous sub-layer and was formulated with a wall-function boundary condition. That is that the boundary condition is prescribed at the innermost part of the logarithmic region of the boundary layer. In order to improve the near-wall behavior of the above stated DRSM, so that the model can be solved all the way down the wall, Shima (1988) introduced near-wall corrections, including the damping function  $f_w$ , to the LRR model.  $f_w$  depends on the wall-distance Reynolds number  $Re_y$  as

$$f_w = \exp\left(-\left(c_{fw}Re_y\right)^4\right), \qquad Re_y = \frac{\sqrt{K}y}{\nu}$$
 (2.11)

where  $c_{fw}=0.015$  and y denotes the wall-normal distance. The value of  $c_{fw}$  was calibrated together with an  $\varepsilon$ -equation, but is re-calibrated to 0.040 in Paper 3 for the use of mod-LRR in combination with a transport equation for the inverse of the turbulence timescale,  $\omega \sim \varepsilon/K$ . The procedure to determine the wall-normal distance in complex geometries is explained in section 2.4 and Paper 5.

Craft & Launder (1996) concluded that the introduction of wall-normal distance was undesirable since "these geometry-specific quantities may be difficult, or impossible, to define uniquely". Instead low-Reynolds number effects were modelled by normalized turbulence lengthscale gradients defined as

$$d_i = \frac{N_i}{0.5 + (N_k N_k)^{0.5}} \quad \text{where } N_i = \frac{\partial \left(K^{1.5}/\varepsilon\right)}{\partial x_i}.$$
 (2.12)

The model was improved further by Craft (1998), with a low-Re expression for the correlation between the fluctuating pressure and velocity  $\overline{pu_i}$ .

If the DRSM is modified to incorporate near-wall damping, this must also be accounted for in the lengthscale determining equation, see section 2.2.

## 2.1.3. Algebraic Reynolds stress model (ARSM)

Introduction of the anisotropy tensor  $a_{ij}$ , yields a separation of the amplituderelated effects from energy redistribution-related effects. The transport equation for the anisotropy tensor can be derived from equations (2.5) and (2.6), see e.g. Sjögren (1997), and the the weak-equilibrium assumption, which states that the advection and diffusion of the anisotropy are negligible, hence

$$\frac{\overline{u_i u_j}}{K} (\mathcal{P} - \varepsilon) = \mathcal{P}_{ij} - \varepsilon_{ij} + \Pi_{ij}$$
(2.13)

An implicit algebraic relation for the Reynolds stress anisotropy tensor is obtained by inserting the definition of the production tensor  $\mathcal{P}_{ij}$  together with

equation (2.8) into equation (2.13).

$$N\mathbf{a} = -A_1\hat{\mathbf{S}} + (\mathbf{a}\hat{\mathbf{\Omega}} - \hat{\mathbf{\Omega}}\mathbf{a}) - A_2\left(\mathbf{a}\hat{\mathbf{S}} + \hat{\mathbf{S}}\mathbf{a} - \frac{2}{3}\operatorname{tr}\{\mathbf{a}\hat{\mathbf{S}}\}\mathbf{I}\right)$$
(2.14)

$$N = A_3 + A_4 \frac{\mathcal{P}}{\varepsilon} \tag{2.15}$$

with the non-dimensionalized mean strain rate denoted  $\hat{\mathbf{S}} = \tau \mathbf{S}$  with turbulence time scale  $\tau = K/\varepsilon$  and the production to dissipation ratio defined as  $\mathcal{P}/\varepsilon \equiv -\text{tr}\{\hat{\mathbf{aS}}\}$ . The  $A_n$ -coefficients are directly related to the  $C_n$ -coefficients in (2.8), see Paper 2.

# 2.1.4. Explicit algebraic Reynolds stress model (EARSM)

The implicit ARSM equation (2.14) can be expressed in an explicit form, see Wallin & Johansson (2000), if  $c_2 = 5/9$  and consequently  $A_2$ =0. The 2D form of the EARSM can be written as

$$\mathbf{a} = \beta_1 \hat{\mathbf{S}} + \beta_2 \left( \hat{\mathbf{S}}^2 - \frac{1}{3} II_S \mathbf{I} \right) + \beta_4 \left( \hat{\mathbf{S}} \hat{\boldsymbol{\Omega}} - \hat{\boldsymbol{\Omega}} \hat{\mathbf{S}} \right)$$
(2.16)

with the functions  $\beta_n$  depend on the second invariants of  $S_{ij}$  and  $\Omega_{ij}$ . This method has also been extended to 3D mean flows where the relation for  $a_{ij}$  consists of five tensor terms for the particular choice of  $c_2 = 5/9$ , see Wllin & Johansson.  $\beta_2 = 0$  for the choice of  $c_2 = 5/9$ , but will have a non-zero contribution close to walls in the low-Re formulation, see section 2.1.5

To simplify the implementation described in chapter 4 and mimic the eddy viscosity formulation of the Reynolds stress, following the work of Wallin & Johansson (2000), the right hand side of the EARSM equation (2.16) is split into two parts as

$$\mathbf{a} = \beta_1 \hat{\mathbf{S}} + \mathbf{a}^{(ex)} \quad \text{or} \quad \overline{u_i u_j} = -2\nu_T S_{ij} + K a_{ij}^{(ex)} + \frac{2}{3} K \delta_{ij}$$
 (2.17)

with  $\nu_T = -\frac{1}{2}\beta_1 K \tau$  corresponding to the eddy-viscosity concept first introduced by Boussinesq. The turbulence timescale is set to  $K/\varepsilon$  or equivalently  $1/(\beta^*\omega)$ .

## 2.1.5. Low-Reynolds number EARSM

To account for low-Re effects, the EARSM was modified by introducing a damping function  $f_1$ , depending on the wall-distance Reynolds number  $Re_y \equiv \sqrt{Ky}/\nu$  as

$$f_1 = 1 - \exp\left(-C_{y1}\sqrt{Re_y} - C_{y2}Re_y^2\right)$$
 (2.18)

with y denoting wall-normal distance. The turbulence time scale is also modified according to Durbin (1993), expressed using either  $\varepsilon$  or  $\omega$  as

$$\tau = \max\left(\frac{K}{\varepsilon}, C_{\tau} \sqrt{\frac{\nu}{\varepsilon}}\right) = \frac{1}{\beta^* \omega} \max\left(1, C_{\tau} \sqrt{\frac{\beta^*}{Re_T}}\right)$$
 (2.19)

where the turbulence Reynolds number is defined as  $Re_T = K/(\omega \nu)$ .

The anisotropy expression from equation (2.17) is hereby modified to include damping as

$$\mathbf{a} = f_1 \beta_1 \hat{\mathbf{S}} + \mathbf{a}^{(ex)} \tag{2.20}$$

with  $f_1$  entering the expression for the turbulence viscosity as  $\nu_T = -\frac{1}{2}f_1\beta_1K\tau$ . The damping function also enters into the extra anisotropy  $\mathbf{a}^{ex}$ .

# 2.2. The 'velocity' and 'lengthscale' equations

In all Reynolds stress closures described in section 2.1, there is still one more quantity needed to close the system of equations. The most widely used is the dissipation rate of turbulence kinetic energy,  $\varepsilon$ , but the value of  $\varepsilon$  when approaching solid walls remains finite. Other quantities mentioned earlier are the turbulence time scale  $\tau$  or its inverse  $\omega$ .

Implementing the six additional transport equations in 3D (four equations in 2D) required for the DRSM or ARSM models will require a large additional computational effort. The use of an EARSM or simple eddy-viscosity model will instead require only two transport equations, one each to determine the velocity and lengthscales of the modelled turbulence. The velocity scale is commonly taken as  $\sqrt{K}$  and the transport equation for the kinetic energy can be derived from equation (2.6) by substituting  $K = \frac{1}{2}\overline{u_iu_i}$ . The choice of auxiliary lengthscale-determining parameter is connected to the dissipation term in the K-equation. The most widely used is the dissipation rate  $\varepsilon$ , but also the inverse of the turbulence time scale  $\omega$  (Wilcox (1993)) and  $\overline{v^2} - f$  by Durbin (1995) have been proven appropriate. Recently, Hanjalić et al. (2004) proposed a modification to the  $\overline{v^2} - f$  by introducing  $\xi = \overline{v^2}/K$ .

We will here focus on the transport equation for  $\omega$  to close the system of equations. The Wilcox (1993) low-Reynolds number formulation was used with near-wall behavior mimicked through the use of the turbulence Reynolds number  $Re_T = K/(\omega \nu)$ . The baseline Wilcox-model for K and  $\omega$  is defined as

$$\frac{\mathrm{D}K}{\mathrm{D}t} = \mathcal{P} - \beta^* \omega K + \frac{\partial}{\partial x_k} \left[ \left( \nu + \frac{\nu_T}{\sigma_K} \right) \frac{\partial K}{\partial x_k} \right]$$
 (2.21)

$$\frac{\mathrm{D}\omega}{\mathrm{D}t} = \mathcal{P}_{\omega} - \beta\omega^{2} + \frac{\partial}{\partial x_{j}} \left[ \left( \nu + \frac{\nu_{T}}{\sigma_{\omega}} \right) \frac{\partial}{\partial x_{j}} \omega \right]$$
 (2.22)

The production terms of turbulence kinetic energy,  $\mathcal{P}$ , and inverse turbulence time-scale,  $\mathcal{P}_{\omega}$ , are formulated as

$$\mathcal{P} = -\overline{u_i u_j} \frac{\partial U_i}{\partial x_i}, \qquad \mathcal{P}_\omega = \gamma \frac{\omega}{K} \mathcal{P}$$
 (2.23)

where the ratio  $\omega/K$  in the definition of  $\mathcal{P}_{\omega}$  also can be expressed as  $1/\nu_T$ . The latter expression can be considered more appropriate when comparing with later proposed formulations of the  $\omega$ -equation. Alternative formulations have been proposed by e.g. Menter (1994), Bredberg *et al.* (2002) and Hellsten (2004). Menter used the eddy viscosity expression and introduced a blending

function between boundary layer flow and outer flow. With the blending function the K- $\omega$  equations are solved close to solid walls and transforms into a K- $\varepsilon$  formulation far away from walls. A similar approach was used by Hellsten, who used the Wallin & Johansson EARSM for the eddy viscosity expression. The Bredberg et al. model originated from a paper by Peng et al. (1997) who derived a K- $\omega$  model from a low-Re K- $\varepsilon$  model. These are described in detail in Paper 4. It is worth mentioning here that all models have added a cross-diffusion term, defined as

$$CD_{\omega} = \sigma_d \frac{1}{\omega} \frac{\partial K}{\partial x_i} \frac{\partial \omega}{\partial x_j}$$
 (2.24)

with  $\sigma_d$  as model parameter, to obtain a consistent behavior of  $\omega$  in the interface between boundary layer and free-stream in external flows. The expression for the turbulence viscosity differ depending on the level of Reynolds stress model. A list of the formulations of  $\nu_T$  is found in Paper 4.

## 2.2.1. Low-Reynolds number K- $\omega$ model

Wilcox (1993) introduced damping functions for the  $\alpha$  and  $\beta^*$ -coefficients in equations (2.21) and (2.22) based on the turbulence Reynolds number  $Re_T$  as

$$\alpha^* = \frac{\alpha_0^* + Re_T/R_k}{1 + Re_T/R_k} \tag{2.25}$$

$$\alpha = \frac{5}{9} \frac{\alpha_0 + Re_T/R_\omega}{1 + Re_T/R_\omega} \frac{1}{\alpha^*}$$
 (2.26)

$$\beta^* = \frac{9}{100} \frac{5/18 + (Re_T/R_\beta)^4}{1 + (Re_T/R_\beta)^4}$$
 (2.27)

$$\beta = 3/40$$

$$\sigma^* = \sigma = 1/2 \quad \alpha_0^* = \beta/3 \quad \alpha_0 = 1/10$$

$$R_k = 6 \quad R_\omega = 2.7 \quad R_\beta = 10$$

$$Re_T = \frac{K}{\omega \nu}$$
(2.28)

The value of  $R_{\beta}$  has been changes from the original value 8.0 determined by Wilcox since Wallin & Johansson (2000) concluded that  $Re_{\beta}=10$  gives better agreement for the mean streamwise velocity profile in the log-layer when using EARSM to model the Reynolds stresses. The near-wall correction coefficients  $\alpha$ ,  $\alpha^*$  and  $\beta^*$  are independent of wall normal distance function, in contrast to the  $f_1$  wall damping function of the EARSM, but instead contain the turbulence Reynolds number, or equivalently the ratio  $K/\omega$ . The near-wall limiting behavior of K and  $\omega$  are proportional to  $y^2$  and  $y^{-2}$  respectively, hence  $Re_T \to 0$  as  $y \to 0$ .

## 2.3. Splitting the $\omega$ -equation

The near-wall behavior of  $\omega$  is singular as  $y\to 0$ , were y is the wall normal distance. One can show that  $K\to y^2$  and  $\varepsilon\to y^0$ . Combining  $\varepsilon=\beta^*\omega K$  with

the asymptotic behavior of  $\beta^* \to \beta/3$ , as seen from eq. (2.27), we obtain the near wall behavior as

$$\omega = \frac{6\nu}{\beta y^2} \quad y^+ < 2.5 \tag{2.29}$$

This, however, causes numerical difficulties since  $\omega \to \infty$  as  $y \to 0$ . The destruction term in the  $\omega$ -equation (2.22) behaves as  $y^{-4}$  and the same is true for the diffusion term. To handle this a splitting of  $\omega$  is desirable. An alternate expression for  $\omega$  is derived in Paper 4 by decomposing  $\omega$  into two parts as

$$\omega = \tilde{\omega} + \omega_{\text{wall}} \tag{2.30}$$

with  $\omega_{\text{wall}}$  is equal to the expression given by equation (2.29) in the whole domain, and  $\tilde{\omega}$  has Dirichlet condition at walls, i.e.  $\tilde{\omega}=0$  for y=0. The method to obtain the wall-normal distance necessary to evaluate  $\omega_{\text{wall}}$  is derived in Paper 5. A short description of the advantages of introducing the decomposition are found below.

Substituting  $\omega = \tilde{\omega} + \omega_{\text{wall}}$  into equation (2.22) transfer the problem from calculating large values of  $\omega$  close to the wall to handling the prescribed function  $\omega_{\text{wall}}$ . Even though  $\omega_{\text{wall}} \sim y^{-2}$ , the second and fourth terms of the right hand side of equation (2.22) are of order  $y^{-4}$ , but

$$\frac{\beta \omega_{\text{wall}}^2 = \frac{(6\nu)^2}{\beta y^4}}{\nu \frac{\partial^2 \omega_{\text{wall}}}{\partial y^2} = 6\nu \frac{6\nu}{\beta y^4}} \Rightarrow \beta \omega_{\text{wall}}^2 = \nu \frac{\partial^2 \omega_{\text{wall}}}{\partial y^2} \tag{2.31}$$

which yields a modified equation for  $\omega$  as

$$\frac{D\tilde{\omega}}{Dt} = \mathcal{P}_{\omega} - \beta \left( \tilde{\omega}^2 + 2\tilde{\omega}\omega_{\text{wall}} \right) + \nabla \left[ (\nu + \sigma\nu_T)\nabla\tilde{\omega} \right] + \nabla \left[ \sigma\nu_T\nabla\omega_{\text{wall}} \right]$$
 (2.32)

The eddy viscosity,  $\nu_T$ , should tend to zero as  $y^3$ , which means that the last term in equation (2.32) vanishes at the wall. In the EARSM context two terms on the right hand side are still singular at the wall ( $\sim y^{-1}$ ). An expression for the near-wall behavior of  $\tilde{\omega}$  is obtained from this condition, and depends on the choice of eddy-viscosity model.

The value of  $\omega_{\rm wall}$  at the boundary now becomes unimportant since it is only necessary to compute the behavior of  $\tilde{\omega}$  as  $y \to 0$ . The near-wall resolution of  $\omega$  is no longer the limiting factor, but rather the resolution of the near-wall peak of K, as concluded i Paper 4. The shear stress model by Menter need two nodes below  $y^+=3$  while Hellsten used an equivalent sand roughness to determine the wall-value of  $\omega$ . For simplicity the boundary value for  $\omega_{\rm wall}$  was set to  $(60\nu)/(\beta y_1^2)$ , where  $y_1$  denotes the distance from the wall to the closest node.

It is shown in Paper 4 that the decomposition can be introduced in most  $\omega$ -equations to date, e.g. Menter (1994), Hellsten (2004) and the low-Re EARSM and K- $\omega$  platform used i Papers 1–4.

#### 2.4. Wall-normal distance function

One of the problems with implementation of turbulence models in CFD codes is that the introduction of damping functions, such as  $f_1$  in equation (2.18), introduces the need to uniquely define the wall distance, which has to be defined specifically for each mesh or flow-case. By introducing the concept of propagating front methods, described by Sethian (1996) this can easily be computed.

The idea of Level Set methods and Fast marching methods was originally used to solve the problem of interface tracking. This was intended to be applicable to e.g. two phase flow or particle tracking. The approach used in this paper was to formulate a scalar equation for  $\phi$ , which in each gridpoint would contain a value equal to the shortest distance to any wall. The wall boundary condition was naturally set to  $\phi_{\text{wall}} = 0$ . This was obtained by defining an equation where the absolute value of the gradient of  $\phi$  must be equal to 1 in all gridpoints, or  $F|\nabla \phi| = 1$ , where F is the propagation speed. The evolution equation of  $\phi$  is therefore formulated

$$\phi_t - (1 - F|\nabla \phi|) = 0 \tag{2.33}$$

with  $\phi_t$  denoting time derivative and where the solution propagates along the wall normal. Ideally F = 1.0, but to damp noise and avoid swallow-tail effects in the numerical scheme, a damping term is added by restating  $F = 1 - \mu_{\phi} \nabla^2 \phi$ .

$$\phi_t - (1 - |\nabla \phi|) = \mu_\phi \nabla^2 \phi \tag{2.34}$$

with  $\mu_{\phi}$  acting as an artificial viscosity, set proportional to the local length of the element sides in the mesh. By letting the  $\phi$ -equation (2.34) reach steady state before any flow calculations were performed,  $\phi$  was used as wall normal distance in the expressions for  $f_1$  (2.18) and  $\omega_{\text{wall}}$  (2.29).

Solving equation (2.34) in any geometry, regardless of complexity or spatial dimensions and with solid wall boundary conditions as stated above, gives the possibility to freely introduce algebraic expressions based on wall normal distance without prior knowledge of the exact domain shape.

See Paper 5 for more details.

#### 2.5. Scalar flux modelling

Once the set of equations governing the flow has been determined, the behavior of additional quantities can be determined by the use of the underlying flow field. One example is the transport of a passive scalar. Typical practical examples of quantities that can be passive scalars are fluid temperature (if buoyancy or heating through friction are neglected), seeding particles in water and pollution transported through the air from industrial areas. The inclusion of the word passive indicates that the scalar is affected by the flow but in turn does not affect the flow. The scalar  $\tilde{\Theta}$  and the governing advection-diffusion equation can be decomposed in to a mean and a fluctuating part,  $\tilde{\Theta} = \Theta + \theta$ , in the same way as the velocity and momentum equations in the fluid model.

Instead of viscosity, there will be a molecular diffusivity, denoted  $\alpha$  and the non-dimensional quantity related to the diffusion is the Prandtl number  $Pr = \nu/\alpha$ . The Reynolds averaged transport equation for  $\Theta$  is

$$\frac{D\Theta}{Dt} = \frac{\partial}{\partial x_i} \left( \alpha \frac{\partial \Theta}{\partial x_i} - \overline{u_i \theta} \right) \tag{2.35}$$

where  $-\overline{u_j\theta}$  denote the scalar flux vector. The most common interpretation of the passive scalar is temperature and this term is then the turbulent heat flux vector.

Similar to the Reynolds stress models described above, the scalar flux vector can obtained by models ranging from complex differential scalar flux models dependent on Reynolds stresses and mean scalar gradient to the simple eddy-diffusivity assumption. Several proposed models have been calibrated against DNS and LES of turbulent channel flows and homogenous shear flows, e.g. by Daly & Harlow (1970), Kim & Moin (1989), Kawamura et al. (1999) and Wikström et al. (2000). Analogous to K and  $\varepsilon$  of the turbulent flow equations are the scalar variance  $K_{\theta} = \frac{1}{2}\overline{\theta^2}$  and its dissipation  $\varepsilon_{\theta}$ . These are also modelled by transport equations, and formulations have been proposed by e.g. Abe et al. (1996), Nagano & Shimada (1996) and Rokni & Sundén (2003).

In Paper 5, the explicit algebraic scalar flux model described by Wikström  $et\ al.$  (WWJ-EASFM), modified by Högström  $et\ al.$  (2001), was used to model passive scalar transport in the asymmetric diffuser. Högström  $et\ al.$  (2001) investigated a variant of the explicit algebraic scalar flux model proposed by Wikström  $et\ al.$  where the time scale ratio r, defined as the ratio between the scalar ant turbulence time scales or

$$r = \frac{\tau_{\theta}}{\tau} = \frac{K_{\theta}/\varepsilon_{\theta}}{K/\varepsilon} \tag{2.36}$$

was assumed to be constant, thus eliminating the need to model transport equations for  $K_{\theta}$  and  $\varepsilon_{\theta}$ . The combined model, described in detail in Paper 5, is defined as

$$\overline{u_i\theta} = K\tau D_{ij}\Theta_{,j} \tag{2.37}$$

with the dispersion tensor  $D_{ij}$  defined as

$$D_{ij} = (1 - c_{\theta 4}) A_{ik}^{-1} \left( a_{kj} + \frac{2}{3} \delta_{kj} \right)$$
 (2.38)

The expression for  $A_{ij}^{-1}$  derived by Wikström  $\ et\ al.$  is explicit in the Reynolds stress anisotropy and gradients of the mean flow and mean scalar fields as

$$A_{ij}^{-1} = \frac{\left(G^2 - \frac{1}{2}Q_1\right)\delta_{ij} - G\left(c_S S_{ij} + c_\Omega \Omega_{ij}\right) + \left(c_S S_{ij} + c_\Omega \Omega_{ij}\right)^2}{G^3 - \frac{1}{2}GQ_1 + \frac{1}{2}Q_2},$$
 (2.39)

with

$$G = \frac{1}{2} \left( 2c_{\theta 1} - 1 - \frac{1}{r} + \frac{\mathcal{P}_K}{\varepsilon} \right) \tag{2.40}$$

$$S_{ij} = \frac{1}{2} \frac{K}{\varepsilon} \left( U_{i,j} + U_{j,i} \right), \quad \Omega_{ij} = \frac{1}{2} \frac{K}{\varepsilon} \left( U_{i,j} - U_{j,i} \right)$$
 (2.41)

$$c_S = 1 - c_{\theta 2} - c_{\theta 3}, \quad c_{\Omega} = 1 - c_{\theta 2} + c_{\theta 3}$$
 (2.42)

$$Q_1 = c_S^2 II_S + c_\Omega^2 II_\Omega, \quad Q_2 = \frac{2}{3} c_S^3 III_S + 2c_S c_\Omega^2 IV$$
 (2.43)

and the second and third order tensor invariants are expressed as

$$II_S = \text{tr}\{\mathbf{S}^2\}, \quad II_{\Omega} = \text{tr}\{\mathbf{\Omega}^2\}, \quad III_S = \text{tr}\{\mathbf{S}^3\}, \quad IV = \text{tr}\{\mathbf{S}\mathbf{\Omega}^2\}.$$
 (2.44)

Again drawing parallels to the EARSM K- $\omega$  platform for the turbulent flow, the dissipation was expressed as  $\varepsilon \sim \omega K$ .  $A_{ij}^{-1}$ . The EASFM described by (2.39)–(2.44), without the Högström et al. modification, was calibrated against DNS in homogenous shear flow, turbulent channel flow at  $Re_{\tau} = 265$  and wake flow. This is compared to a eddy-diffusivity model (EDM) where the scalar flux vector was assumed proportional to the mean scalar gradient,  $\overline{u_i\theta} \sim \partial\Theta/\partial x_i$ .

# CHAPTER 3

# Numerical treatment

In this chapter the numerical aspects will be described in some detail. As a prelude, we will briefly recapitulate the finite element method, We will then describe the solver used for the Navier-Stokes equations and some numerical issues in the K- $\omega$  and EARSM formulations.

The finite element method was first developed to solve problems in structural mechanics, but was also adopted to solve fluid mechanic problems. In finite difference or finite volume methods, one takes the existing equations and replace derivatives with appropriate discrete counterparts containing values of unknowns at a number of adjacent points. The finite element approach is somewhat different in that the mathematical problem is converted to variational form and an approximate solution is found as a sum of a finite number of base functions.

## 3.1. Finite Element Method (FEM)

To introduce the weak form of a partial differential equation, PDE, let us look at a very simple example, the heat equation on vector form with Neumann boundary condition.

$$\frac{\partial \theta}{\partial t} = \alpha \nabla^2 \theta \text{ in } \Omega \tag{3.1}$$

with Dirichlet boundary condition

$$\theta = 0 \text{ on } \Gamma_0$$
 (3.2)

and Neumann boundary condition

$$\alpha \frac{\partial \theta}{\partial n} = q \text{ on } \Gamma_1 \tag{3.3}$$

In (3.1)  $\theta$  denotes the temperature,  $\alpha$  is a (constant) thermal diffusivity and in (3.3) n is the wall normal direction. Introducing a test function  $\eta \in V$ , where V is a given set of admissible functions, and integrating over the domain  $\Omega$  gives

$$\int_{\Omega} \eta \frac{\partial \theta}{\partial t} dV = \int_{\Omega} \alpha \eta \nabla^2 \theta dV$$
 (3.4)

Partial integration of the right hand side of (3.4) yields: Find  $\theta \in V$  such that

$$\int_{\Omega} \eta \frac{\partial \theta}{\partial t} d\mathbf{V} = -\int_{\Omega} \alpha \nabla \eta \nabla \theta d\mathbf{V} + \int_{\Gamma_1} \eta q d\mathbf{S} \qquad \eta \in V$$
 (3.5)

Equation (3.5) is the weak form of the PDE (3.1) with the Neumann boundary condition (3.3) incorporated in the boundary integral obtained from equation (3.5) by using Greens formula.

The introduction of V as a set of admissible functions needs some further explanation. For the volume integral to be bounded on  $\Omega$ , the test function has to be differentiable and square integrable on  $\Omega$ , hence V is the Hilbert space  $H_0^1$  defined as

$$H_0^1(\Omega) = \{ \eta \in H^1(\Omega) : \eta = 0 \text{ on } \Gamma_0 \}$$

with

$$H^1(\Omega) = \{ \eta \in L_2(\Omega) : \frac{\partial \eta}{\partial x_i} \in L_2, i = 1, ..., d \}$$

$$L_2(\Omega) = \{ \eta : \int_{\Omega} \eta^2 d\mathbf{V} < \infty \}$$

and d denoting the number of spatial dimensions.

To obtain an approximate solution of these equations, the continuous domain  $\Omega$  is divided into a finite set of m elements, forming the discretized domain  $T_h$ . In the 2D case with triangular elements the discretized domain is the set  $T_h = \{K_1, \ldots, K_m\}$  of  $K_m$  non-overlapping triangles  $K_i$ . The corners of these triangles form a set of n nodes of the mesh. Also, let n denote the longest element side found among the elements in n. The space n0 denotes the space consisting of piecewise polynomials. Even more specifically, let n1 n2 denote the subspace of piecewise linear test functions.

For a triangle K with the nodes  $N_j$ , j=1,2,3, the base functions  $\lambda_i \in P^1$  satisfy

$$\lambda_i(N_i) = \delta_{ij} \tag{3.6}$$

or put into words, the base function for node i is equal to 1 on the node and 0 on any other node. From this,  $\eta(\vec{x}) \in P^1$  is then represented as

$$\eta(\vec{x}) = \sum_{i=1}^{3} \eta(N_i) \lambda_i(\vec{x}) \tag{3.7}$$

The exact shape of the base function between nodes depend on the needed accuracy. The most widely used types are piecewise polynomials with constant  $(P^0)$ , linear  $(P^1)$  or quadratic  $(P^2)$  behavior between nodes. For a detailed description, see Gresho & Sani (1998).

In the computations of the turbulent channel flow and asymmetric diffuser described in chapter 5, linear  $P_1$  elements have been used for all equations. This was possible through the introduction of a fractional step method, described in section 3.2.1.

# 3.2. Weak form of the Navier-Stokes equations

The incompressible Navier-Stokes equations have been defined in chapter 2, and are restated here on tensor form for convenience.

$$\frac{\partial \tilde{u}_i}{\partial t} + \tilde{u}_j \frac{\partial \tilde{u}_i}{\partial x_j} = -\frac{1}{\rho} \frac{\partial \tilde{p}}{\partial x_i} + \frac{\partial}{\partial x_j} (2\nu \tilde{s}_{ij}) \text{ in } \Omega$$
(3.8)

$$\frac{\partial \tilde{u}_i}{\partial x_i} = 0 \tag{3.9}$$

with boundary conditions

$$\tilde{u}_i = u_i^0 \text{ on } \Gamma_0 \tag{3.10}$$

$$\tilde{u}_i = 0 \text{ on } \Gamma_1$$
 (3.11)

$$n_j \frac{\partial \tilde{u}_i}{\partial x_j} = 0, \ \tilde{p} = 0 \ \text{on } \Gamma_2$$
 (3.12)

with indices 0, 1 and 2 on  $\Gamma$  representing inlet, solid wall and outlet boundaries respectively. To obtain a weak form of (3.8)-(3.12) the test function  $\eta \in V$  was introduced as explained in the previous section and integrated over the domain. Find  $\tilde{u}_i \in V$  such that

$$\int_{\Omega} \eta \frac{\partial \tilde{u}_{i}}{\partial t} d\mathbf{V} + \int_{\Omega} \eta \tilde{u}_{j} \frac{\partial \tilde{u}_{i}}{\partial x_{j}} d\mathbf{V} + \int_{\Omega} \eta \frac{\partial \tilde{p}}{\partial x_{i}} d\mathbf{V} = \int_{\Omega} \eta \frac{\partial}{\partial x_{j}} 2\nu \tilde{s}_{ij} d\mathbf{V} \quad \forall \eta \in V \quad (3.13)$$

$$\int_{\Omega} \eta \frac{\partial \tilde{u}_i}{\partial x_i} dV = 0 \tag{3.14}$$

or equivalently, expanding  $\tilde{s}_{ij} = \frac{1}{2} (\partial \tilde{u}_i/\partial x_j + \partial \tilde{u}_j/\partial x_i)$ 

$$\int_{\Omega} \eta \frac{\partial \tilde{u}_{i}}{\partial t} + \eta \tilde{u}_{j} \frac{\partial \tilde{u}_{i}}{\partial x_{j}} dV = -\int_{\Omega} \eta \frac{\partial \tilde{p}}{\partial x_{i}} dV 
- \int_{\Omega} \nu \frac{\partial \eta}{\partial x_{j}} \left( \frac{\partial \tilde{u}_{i}}{\partial x_{j}} + \frac{\partial \tilde{u}_{j}}{\partial x_{i}} \right) dV + \int_{\Gamma} \nu \eta \left( \frac{\partial \tilde{u}_{i}}{\partial x_{j}} + \frac{\partial \tilde{u}_{j}}{\partial x_{i}} \right) n_{j} dS$$
(3.15)

$$\int_{\Omega} \eta \frac{\partial \tilde{u}_i}{\partial x_i} dV = 0$$
(3.16)

Since  $\eta = 0$  on  $\Gamma_{0,1}$  and  $\partial u_i/\partial n = 0$  on  $\Gamma_2$ , the boundary integrals are eliminated.

## 3.2.1. Fractional step method in time

Time derivatives are approximated by a finite difference,

$$\frac{\partial \tilde{u}_i}{\partial t} \to \frac{\tilde{u}_i^n - \tilde{u}_i^{n-1}}{\Delta t} \tag{3.17}$$

with  $\tilde{u}_i^n$  as the unknown for which the equation is solved,  $\tilde{u}_i^{n-1}$  denoting the solution at the previous time step and  $\Delta t$  the time increment.

Guermond & Quartapelle (1997) introduced an incremental fractional step method where the velocity field at time iteration n is obtained by first calculating an intermediate velocity field  $\hat{u}_i^n$ . For convenience, let N and L denote the advection and diffusion terms of equation (3.15) at this moment. The time

discretized form of the Navier-Stokes equations, combining equations (3.15), and (3.17), then take the form

$$\int_{\Omega} \eta \frac{\hat{u}_{i}^{n} - \hat{u}_{i}^{n-1}}{\Delta t} dV + N =$$

$$- \int_{\Omega} \eta \frac{\partial \tilde{p}^{n-1}}{\partial x_{i}} dV - \int_{\Omega} \eta \frac{\partial}{\partial x_{i}} \left( \tilde{p}^{n} - \tilde{p}^{n-1} \right) dV + L$$
(3.18)

where the pressure at time n is rewritten as  $\tilde{p}^n = \tilde{p}^{n-1} + (\tilde{p}^n - \tilde{p}^{n-1})$ . Using the same base function for velocity and pressure is always unstable (Gresho & Sani (1998)), but stabilization can be achieved by 'regularizing' the incompressibility constraint by a adding a laplacian of the pressure to the right hand side.

$$\int_{\Omega} \eta \frac{\partial \tilde{u}_{i}^{n}}{\partial x_{i}} dV = \int \eta \epsilon_{p} \frac{\partial^{2} \tilde{p}^{n}}{\partial x_{i} \partial x_{i}}$$
(3.19)

with  $\epsilon_p$  as a strictly positive regularization parameter of order  $O(h^2)$ .

The fractional step method divides equation (3.18) into a three step procedure. First the viscous step, accounting for the viscous diffusion and the convection, then a Poisson equation for the pressure update and finally the convection step determining the divergence free end-of-step velocities. The intermediate step velocity  $\hat{u}_i^n$ , introduced to equation (3.18), will ultimately be solved for through

$$\int_{\Omega} \eta \frac{\hat{u}_{i}^{n} - \hat{u}_{i}^{n-1}}{\Delta t} dV + \int_{\Omega} \eta \hat{u}_{j}^{n-1} \frac{\partial \hat{u}_{i}^{n}}{\partial x_{j}} dV =$$

$$- \int_{\Omega} \eta \frac{\partial}{\partial x_{i}} \left( 2\tilde{p}^{n-1} - \tilde{p}^{n-2} \right) dV - \int_{\Omega} \frac{\partial \eta}{\partial x_{j}} 2\nu \hat{s}_{ij}^{n} dV \tag{3.20}$$

yielding the equation for the fractional time step velocity only. After solving for  $\hat{u}_i^n$  the continuity equation is replaced by the Poisson pressure equation by taking the gradient of equation (3.22) and substituting the end-of-step velocity expression from the continuity equation (3.19), hence

$$\int_{\Omega} \eta \frac{\partial^2}{\partial x_i \partial x_i} \left( \tilde{p}^n - \tilde{p}^{n-1} \right) dV = \frac{1}{\Delta t} \left[ \int_{\Omega} \eta \frac{\partial \hat{u}_i^n}{\partial x_i} dV + \int_{\Omega} \eta \epsilon_p \frac{\partial^2 \tilde{p}^n}{\partial x_i \partial x_i} dV \right]$$
(3.21)

The end-of-step velocity is finally obtained from

$$\int_{\Omega} \eta \frac{\tilde{u}_{i}^{n} - \hat{u}_{i}^{n}}{\Delta t} dV = -\int_{\Omega} \eta \frac{\partial}{\partial x_{i}} \left( \tilde{p}^{n} - \tilde{p}^{n-1} \right) dV$$
 (3.22)

The split scheme now consists of the three steps above:

- 1. Solve equation (3.20) for  $\hat{u}_i^n$ . Note that the convection and viscous terms are solved implicitly using a GMRES solver.
- 2. Solve (3.21) for  $\tilde{p}^n$  using a preconditioned CG solver.
- 3. Calculate corrected velocities  $\tilde{u}_i^n$  from (3.22)

As shown by Guermond & Quartapelle (1997), this procedure greatly reduces spurious pressure waves since  $\tilde{u}_i^n$  was eliminated from (3.20).

# 3.3. Boundary conditions

No slip conditions are used at solid walls, implying that mean velocities and Reynolds stresses are zero at walls. The use of the  $K-\omega$  formulation with decomposed  $\omega$ -equation as turbulence model enabled integration down to the walls and consequently  $K|_{\text{wall}} = \tilde{\omega}|_{\text{wall}} = 0$ . The boundary value of  $\omega_{\text{wall}}$  can be set to an arbitrary large number since it is, by definition, singular on the boundary and the behavior up to the last grid point is prescribed.

The set of unknowns are all (except the pressure) described on the inlet, while at outlet boundaries the Neumann condition is applies, defined by equation (3.12). The pressure is set equal to zero on the outlet.

## 3.4. Distance function

To obtain the distance to the closest wall at any point in the computational domain, regardless of the shape of the domain, a distance function was computed. The derivation and background is found in section 2.4 as well as Paper 5. The differential equation is restated here for convenience, with  $\phi$  denoting the wall normal distance.

$$\frac{\partial \phi}{\partial t} - (1 - |\nabla \phi|) = \mu_{\phi} \nabla^2 \phi \tag{3.23}$$

With the 2-norm of the gradient expressed as  $|\xi| = \xi^2/\sqrt{\xi^2}$  and replacing  $\xi$  with  $\partial \phi/\partial x_j$ , the variational form of equation (3.23) was stated as

$$\int_{\Omega} \eta \frac{\phi^{n} - \phi^{n-1}}{\Delta t} dV - \int_{\Omega} \eta dV + \int_{\Omega} \eta \left[ \frac{\frac{\partial \phi^{n}}{\partial x_{j}} \frac{\partial \phi^{n-1}}{\partial x_{j}}}{\sqrt{\frac{\partial \phi^{n-1}}{\partial x_{j}} \frac{\partial \phi^{n-1}}{\partial x_{j}} + \epsilon_{\phi}}} \right] dV = 
- \int_{\Omega} \mu_{\phi} \frac{\partial \phi^{n}}{\partial x_{j}} \frac{\partial \eta}{\partial x_{j}} dV$$
(3.24)

The parameter  $\epsilon_{\phi} \ll 1$  is introduced to avoid dividing by zero at peaks and ridges in the  $\phi$ -field, where  $|\phi|$  is close to 0.  $\phi$  was first computed by solving the time dependent equation (3.24) to steady state. Since (3.24) is independent of the flow, the solution for the distance function was used without further updates throughout the solution of the flow problem. The propagation speed of the distance function is equal to one, hence the time needed to reach steady state equals half the estimated maximum distance between two solid walls. The computational effort required for this procedure is negligible compared to the effort to obtain the flow solution.

## CHAPTER 4

# Automated code generation

As the system of equations gets more and more complex, the derivation of the equations and the conversion from partial differential equations to a working computer code can be very time consuming. Also the risk of introducing errors is high, especially as the dimensions of the problem increases. By using symbolic computation coupled with automated code generation, the possibility arises to express the equations in more general and symbolic format.

Using the femLego toolbox, based on the work of Amberg et al. (1999), together with Maple, the partial differential equations, the boundary conditions and initial conditions as well as the method of solving each equation can all be specified in a Maple worksheet. The finite element code is generated, using the femLego toolbox, from that sheet. Maple presents the equations in a readable and easily edited format and it is possible to put the documentation of the mathematical part of the project within the script. It also gives the advantage of deriving the equations in the language of applied mathematics.

# 4.1. Example PDE: The heat equation

The heat equation has been defined (3.1-3.3) and put on weak formulation (3.5) in the previous chapter. It is here used to show how easy and flexible the environment can be to work with. Though we will only describe the solution procedure of a single equation PDE, it is easily expanded to systems of equations.

The computational domain in this example is a 2D rectangle with a heated left wall ( $\Theta = T_1$  on  $\Gamma_1$ ) and a cold isothermal object inside ( $\Theta = T_2$  on  $\Gamma_2$ ). The horizontal walls are insulated ( $\partial\Theta/\partial n=0$  on  $\Gamma_3$ ) and the left wall has a prescribed heat flux ( $\alpha\partial\Theta/\partial n=q$  on  $\Gamma_4$ ). The geometry is shown in figure 4.1 and the Maple worksheet for the complete problem in figure 4.2. The necessary steps and definitions in the process are described in section 4.2.

# 4.2. Description of the femLego syntax

4.2.1. Deriving the equations

With the help of the tensor operator package in femLego the equations can be formulated in tensor form and complex tensorial expressions are easily defined. The nabla operator  $\partial/\partial x_j$  is implemented as nab(...)[j] and the Einstein summation rule is invoked by using the multiplication operator &t. The weak

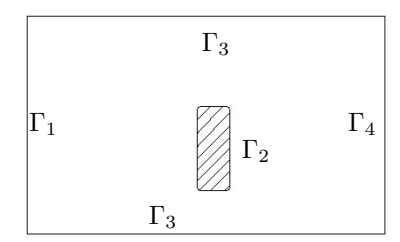


FIGURE 4.1. Domain and boundary notations used in the heat equation example.

form of the equation is given by equation (3.5), which is restated here for convenience.

$$\int_{\Omega} \eta \frac{\partial \Theta}{\partial t} dV = -\int_{\Omega} \alpha \nabla \eta \nabla \Theta dV + \int_{\Gamma_4} \eta q dS \quad \eta \in V$$
 (4.1)

This is inserted under the heading 'Specify PDE' in figure 4.2. Integrations over volumes are denoted ElementInt() and over boundaries BoundaryInt(). Notice the use of &t to express

$$\int_{\Omega} \alpha \nabla \eta \cdot \nabla \Theta dV \tag{4.2}$$

as

ElementInt(alpha\*nab(eta(x,y))[j] & t nab(theta(x,y))[j])

which, after evaluating gradients and the scalar multiplication, generates the output

$$-\text{ElementInt}\left(\alpha\left(\left(\frac{\partial}{\partial x}\eta(x,y)\right)\left(\frac{\partial}{\partial x}\Theta(x,y)\right) + \left(\frac{\partial}{\partial y}\eta(x,y)\right)\left(\frac{\partial}{\partial y}\Theta(x,y)\right)\right)\right)$$

The time derivative is approximated as a simple finite difference. Notice the use of  $\Theta(x,y)$  as the temperature at the new time step to be computed and  $\Theta(x,y)$  as the temperature from the previous time step. In this example the laplacian of the right hand side is expressed in terms of  $\Theta(x,y)$ , which makes this an implicit term.

Equations, as well as boundary and initial conditions, may contain explicit space and time dependencies, which are introduced using x, y or time in the expressions. Some equations are simple relations that only need copying of node values e.g.  $\omega_{\rm wall}$ . For such expressions CopyEq(...) can be used instead of ElementInt.

## 4.2.2. Defining the input lists

Under the heading 'Define input lists' in figure 4.2, the equations that have been defined are stored, together with the names of the unknowns etc. in a set of lists that are used repeatedly as input in the sections below. The equations are stored in the list eq\_list, which also specifies the order in which the equations are solved in the case of a system of equations. The corresponding

unknown for which each equation is solved for is listed in unknown\_list. The variable name of the known solution from the previous time step is stored in old\_unknown\_list. The definitions of the two unknown-lists correspond to the notations  $\Theta^n$  and  $\Theta^{n-1}$  used in chapter 3.

The list params\_list specifies scalar parameters introduced in the equations whose values have to be set before each calculation. This is convenient for material properties of the fluid or boundary and initial values.

# 4.2.3. Specifying boundary and initial conditions

The Dirichlet boundary conditions are specified under the next heading in figure 4.2, named just that: 'Dirichlet boundary conditions'. The list DBCeq contains an expression for each unknown which have non-zero Dirichlet boundary conditions at any boundary. The parameter qBCval is used as a flag to associate boundary conditions with different parts of the boundary. Several Dirichlet conditions for one unknown can be specified by the use of tswitch(qBCval-n). n = 1, ..., N denotes numbers specified in the description of the mesh that identify different parts of the boundary.

The need to lock only a single nodal value by a Dirichlet condition can arise, for instance for the pressure in an internal flow. This is made available by the command SinglePoint(unknown) for inclusion in DBCeq.

The expressions for the initial conditions are found under the heading 'Specify initial conditions' in figure 4.2. These are specified in the same way as the entries in the DBCeq-list.

# 4.2.4. Pre and post processing

Generation of the unstructured mesh and the boundary condition list for each boundary and unknown have to be done separately. So far, the femLego can read meshes created in Femlab or Gambit, but the open structure of femLego gives the possibility to define generic import routines to accommodate other mesh generators. In the section 'Specify input' in figure 4.2 femLego commands are called that incorporate the code to read meshes and input in a specific format.

A parameter file named indata\_sample, containing among other things the parameters listed in params\_list is produced. An example of the necessary and auxiliary quantities can be found in table 4.1. The three first lines controls the input, output, convergence tolerance and time parameters. The following lines are added depending on the number of entries in the params\_list.

The post processing of data is not included in femLego, but output functions support export of the results to be read by Femlab, Matlab, AVS or OpenDX. The code that creates output for a specific application is included by executing the appropriate femLego command under the heading 'Specify output'.

heat	empty		file save: outplotfile, infile
1.E-8	1000		tolerance and maxiter in cg:
0.1	25.	5.	dt, endtime, plottime
1.96E-5	15.4		alpha, T1
4.	2.		T2, Q

Table 4.1. Indata file with parameters defined in figure 4.2.

# 4.2.5. Creating the solver

Under the heading 'Specify linear algebra solvers', the methods used to solve the linear system of equations that arise are specified. Each equation is solved one after the other in a split manner. The list solve\_list specifies the linear solver that is to be used for each equation, in the order they are given in eq\_list. Typical choices are the preconditioned conjugate gradient (iccg) method for symmetric positive definite equations, or the generalized minimum residual (gmres) method for non-symmetric equations. copy is used for an equation defined with the CopyEq() keyword. This is useful in the case where a variable is given by a simple algebraic expression which can be computed at each node.

The full set of fortran files needed to compile the code are generated by the mkFem(...) command, under the heading 'Creating the core of the solver'. Here the name of the base function is specified together with a filename calling a file that contains all the definitions that specify the particular finite element.

Once the code has been compiled, it can be executed together with an indata file an a mesh file in the proper formats described above.

```
c > read(femLego);
■ Specify PDEs
  heateq := ElementInt \left(\frac{\eta(x,y)(\theta(x,y) - \theta \theta(x,y))}{1 + \theta \theta(x,y)}\right)
         -\text{ElementInt}\left(\alpha\left(\left(\frac{\partial}{\partial x}\eta(x,y)\right)\left(\frac{\partial}{\partial x}\theta(x,y)\right) + \left(\frac{\partial}{\partial y}\eta(x,y)\right)\left(\frac{\partial}{\partial y}\theta(x,y)\right)\right)\right) + \text{BoundaryInt}(\eta(x,y)Q)
■ Define input lists
  c > eq_list:= [heateq]:
c > unknown list:= [theta(x,y)]:
c > old_unknown_list:= [theta0(x,y)]:
c > parāms_list:= [alpha,TI,T2,Q]:
■ Dirichlet boundary conditions
  > DBCeq:= theta(x,y)=11-tswitch(qBCval-1)+T2\tswitch(qBCval-2);

DBCeq:=\theta(x,y)=T1\tswitch(qBCval-1)+T2\tswitch(qBCval-2)

> mkDirBC([DBCeq],unknown_list,old_unknown_list, params_list,'2DP1_gsq_bsf'):
                                                         adddbc
                                                         SPdirb
■ Specify initial conditions
  value 0:
value 0:
> mkIC([ theta(x,y)=T1 ], unknown_list, params_list , '2DP1_gsq_bsf');
■ Specify input
  ^{\mbox{\tiny L}}> # get files to read input from femlab. Input from Gambit also available; _{\mbox{\tiny J}}> getFemLabInput(params_list):
                                                     indata sample
■ Specify output
c > FemLabPlot([theta(x,y)],[temperature],unknown_list);
■ Specify linear algebra solvers
  dosolve
                                                         solve
■Create the core of the solver
  c > # create residual computations etc:
    > size_parameters:=mkFem(eq_list, unknown_list,
    old_unknown_list, params_list, eta(x,y), '2DP1_gsq_bsf');
                                                  check include/size.h:
                                                        nvar: .1
                                                        nobf:,3
```

FIGURE 4.2. Maple worksheet for solving the heat equation.

## CHAPTER 5

# Results

In this chapter a short introduction to the asymmetric diffuser geometry is made. A summary of the results from Papers 1–4 are presented, comprising mean flow behavior, turbulence quantities, mean passive scalar and scalar flux components.

# 5.1. Decomposition of $\omega$

In the numerical solution of two-equation models, the requirement of the nearwall node resolution, usually associated with the use of the  $\omega$ -equation as lengthscale determining equation, is very high due to the asymptotic nearwall behavior of  $\omega \sim y^{-2}$ . This requirement has been substantially relaxed by the introduction of a decomposition of  $\omega = \tilde{\omega} + \omega_{\rm wall}$ . The  $y^{-2}$  dependency is included in  $\omega_{\rm wall}$  and  $\tilde{\omega}$  is the property that is solved. This is shown in Paper 4 where three  $\omega$ -formulations are modified to include the decomposition. The three formulations are the low-Re Wilcox (1993), Menter (1994) SST and Hellsten (2004). The near wall behaviors of the two parts of  $\omega$  in turbulent channel flow at  $Re_H = 40~000$  are shown in figure 5.1, results from. At  $y^+ = 2.5$  the ratio  $\omega_{\rm wall}/\tilde{\omega} = 20$ , satisfying the condition that  $\omega_{\rm wall}$  should be the dominating term for  $y^+ < 2.5$ .

The slope of  $\tilde{\omega}$  in the near-wall region where  $\omega_{\rm wall}$  is dominant is determined by the relation

$$\tilde{\omega} \approx -\frac{\gamma}{2\beta} a_{ij} S_{ij} \sim d^n \quad \text{as} \quad d \to 0$$
 (5.1)

and n=0,1,2 depending on the choice of anisotropy formulation. The computed near-wall behavior of  $\tilde{\omega}$  for different models is compared to the analytical relation (5.1) in figure 5.2. It was concluded in Paper 4 that the first wall-normal node,  $y_1^+$ , could be placed at  $y^+=5$  if the decomposition was employed. It was also shown that this distance was limited by the resolution of K rather than  $\tilde{\omega}$ .

# 5.2. Plane asymmetric diffuser geometry

The turbulent flow in an asymmetric diffuser contains a separated region along the inclined wall if the inclination angle is large enough. The geometry was initially used in experiments and computations by Obi *et al.* (1993b). Later the ERCOFTAC organisation defined this as a standard test case based on the geometry used by Obi. The diffuser geometry consists of three main parts.

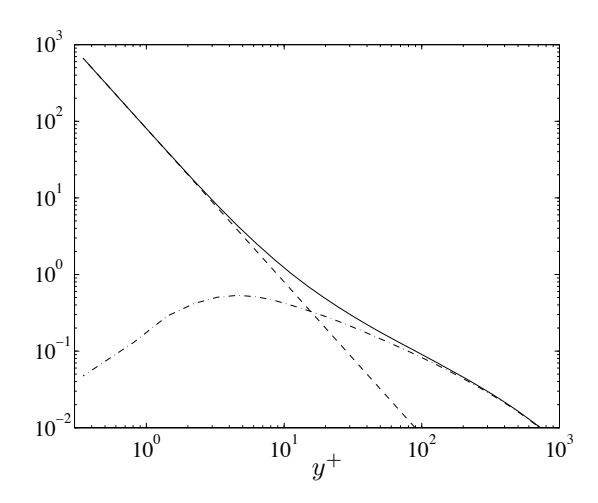


FIGURE 5.1. The magnitudes of  $(-\cdot -)$   $\tilde{\omega}$ , (--)  $\omega_{\text{wall}}$  and (--)  $\omega$  from the wall to the centerline.

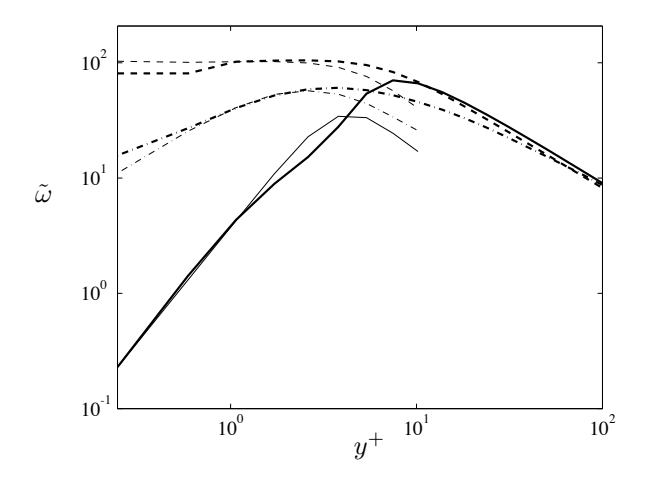


FIGURE 5.2.  $\tilde{\omega}$  close to the wall for Menter SST (—), Hellsten (– –) and Wilcox (– · –). Thick lines denote  $\tilde{\omega}$  and thin lines the behaviour using the relation equation (5.1), *i.e.*  $d^n$ , n=0,1,2 respectively, as  $d\to 0$ .

First, a plane inlet channel long enough to achieve a fully developed turbulent profile before entering the second part, the diffuser. An inlet length of 110H has been used in the present calculations, agreeing with the ERCOFTAC guidelines. The diffuser starts with an upstream corner on one of the walls, with corner radius of 9.7H and ends with an identical corner and an exit channel with a length of at least 60H. The expansion ration between inlet and exit channel is 4.7H.

The challenge for turbulence models is to predict the strong asymmetry in the velocity profile and the location of the separation and reattachment points of the separated region in this geometry. The separation point is pressure induced, in contrast to other bench mark geometries such as the 2D backward-facing step or the 3D surface mounted cube, where the separation points are defined by sharp edges in the geometry.

Experiments were initially performed by Obi et al. (1993a) using 10° inclination angle and a Reynolds number of  $Re_H = 40~000$  based on the inlet bulk streamwise velocity  $U_b$  and channel height H. Experiments have also been carried out, using 10°, by Buice & Eaton (2000). The 10° geometry has been used as a test case for turbulence models by ERCOFTAC, with a workshop comprising of K- $\varepsilon$  and K- $\omega$  models. A large eddy simulation (LES) has also been reported by Kaltenbach et al. (1999) at  $Re_{\tau} = 1~000$  based on half inlet channel height and inlet channel friction velocity. The results from LES showed close agreement with experimental data from Buice & Eaton for the mean velocity profiles, while a discrepancy was found in the location of the reattachment point. Kaltenbach concluded that subgrid-scale modelling played an essential role since sub-grid stresses contributed to up to 8% of the total shear stresses. Apsley & Leschziner (2000) found that strain dependent coefficients and anisotropy resolving models are needed to correctly capture the diffuser flow. In their study, they compared eddy-viscosity models, anisotropy resolving models as well as differential Reynolds stress models. Iaccarino (2000) used commercial CFD codes, implementing the  $\overline{v^2} - f$  model proposed by Durbin (1995) and the K- $\varepsilon$  model. The K- $\varepsilon$  model was unable to predict a separation region, while the extent agreed within 6% for the  $\overline{v^2} - f$  model compared with data from both Obi et al. and Buice & Eaton.

Computations for both inclination angles have been performed with the full differential (DRSM) as well as explicit algebraic Reynolds stress models (EARSM) and a comparison of the size of the separated region obtained in experiments and in the computations is found in Paper 3.

Experimental data and computations in an asymmetric diffuser at  $8.5^{\circ}$  angel are presented in Paper 1. The smaller angle of  $8.5^{\circ}$  was used in the experiments reported in Paper 1 to obtain a separation region that would be more sensitive to control efforts and to facilitate the achievement of a high degree of spanwise homogeneity. The turbulence model used was the EARSM of Wallin & Johansson (2000) based on a platform consisting of the K- $\omega$  equations of the Wilcox (1993) model. Both models included low-Reynolds number corrections as described in chapter 2.

An additional computational study of the diffuser with heated walls has been done in order to study the modelling of turbulent transport of a passive scalar, such as temperature. The explicit algebraic scalar flux model by Wikström *et al.* (2000) with modifications by Högström *et al.* (2001), described in Paper 2 has been compared to an eddy diffusivity model (EDM) in the asymmetric diffuser for several boundary conditions.

# 5.3. Diffuser flow

The flow entering the diffuser stays attached to both walls until a large separation region forms on the inclined (upper) wall. This will contribute to a concentration of high streamwise velocity near the straight wall and affects the pressure recovery along both walls.

The streamwise and wall-normal extents of the separation region is defined by the dividing streamline,  $\Psi_0$ , which in turn is defined by the streamfunction  $\Psi$  as

$$\Psi = \frac{1}{U_b H} \int_0^y U(y) dy \tag{5.2}$$

with U denoting the mean streamwise velocity. Computations presented in Paper 1 indicate that the limiting angle for a separation bubble to occur is 8°. This must be regarded only as an indication, since the size of the separation region in severely underestimated by computations when compared to experimental data for the 8.5° case. Figure 5.3 shows a comparison of the extent of the separation region, found in Paper 3, between three variants of the EARSM, the DRSM and experiments at both 8.5° and 10°. It can be observed that the wall-normal extent of the separation region found in the experimental data is 60% larger than any extent predicted by the flow model. By using the same  $\omega$ -equation and pressure-strain rate modelling in the DRSM as in EARSM 3, it was shown that the algebraic assumption is a viable approach in this case. The

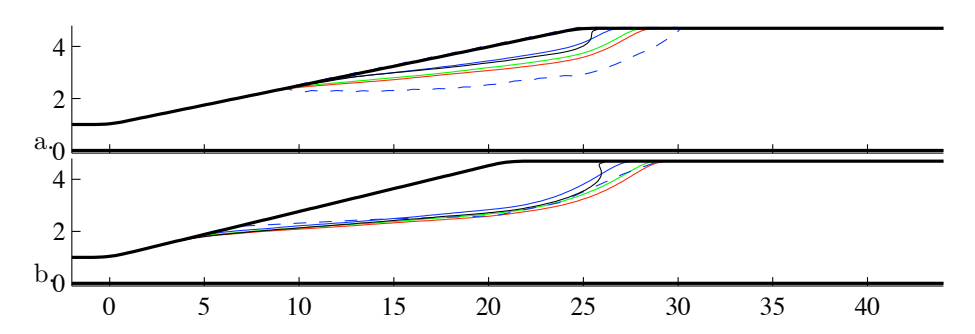


FIGURE 5.3. Size of separation region at a)  $8.5^{\circ}$  and b)  $10^{\circ}$  predicted by (—) standard WJ EARSM, (—) EARSM type 2, (—) EARSM type 3 and (—) DRSM. Dashed lines indicate region from experiments a) Paper 1 and b) Buice & Eaton (2000)

main problem for any turbulence model has been to capture the magnitude of the (negative) velocity in the separation region observed in the experiments, see e.g. Hellsten & Rautaheimo (1999) and Paper 1.

The mean streamwise velocity component in the 8.5° diffuser is shown in figure 5.4a, where the asymmetry is reasonably well predicted. Standard eddy-viscosity models show much more symmetric velocity profiles, see Hellsten & Rautaheimo (1999). However, the discrepancy between experiments and computation is evident considering the details close to the walls. The peak velocity outside of the separation region occurs closer to the walls in the experiments, again indicating a larger separation region. The development downstream of the diffuser shows how the skewed velocity profile is maintained in the computations while a new symmetric profile is recovered in the measurements. The agreement in wall-normal position of the peak velocity was improved by the modified EARSM described in paper 3.

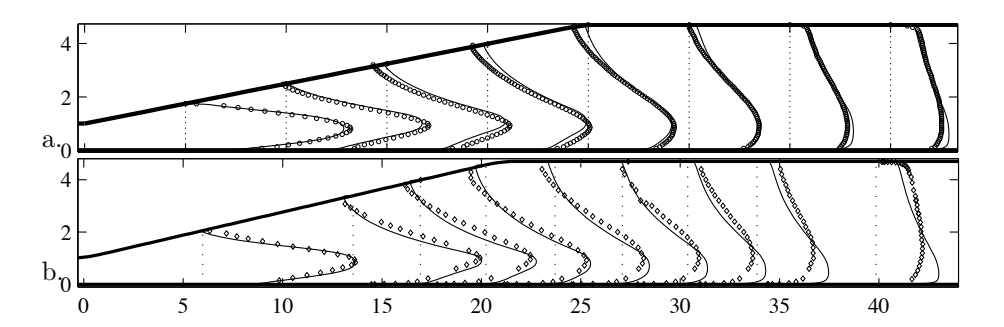


FIGURE 5.4. Streamwise velocity  $10U/U_b$  from EARSM for a) the 8.5° case and b) the 10° case,  $10U/U_b$ . Experiments ( $\square$  in Paper 1 for a) and ( $\circ$ ) data from Buice & Eaton (2000) in b)).

## 5.3.2. Turbulence quantities

The general behavior of the turbulent quantities are shown in figure 5.5, where the streamwise turbulence kinetic energy  $K/U_b^2$  and variances  $\overline{u^2}/U_b^2$  and  $\overline{v^2}/U_b^2$  are shown compared to experiments in the 8.5° diffuser. The agreement for the kinetic energy between computations and experiments is satisfactory in the beginning of the diffuser, while the computations underestimate K from x/H=20 and downstream. Looking at each stress component, the main contribution to this behavior for the standard EARSM is found in the  $\overline{u^2}$ -component. The large values of  $\overline{u^2}$  observed in the near-wall region in the experiments are not apparent in the computations, while the agreement for the  $\overline{v^2}$ -components is satisfactory. It was observed in Paper 1 that  $\mathcal{P}$ , the production of K, showed good agreement with experiments, indicating that the diffusion model may have to be changed to improve the agreement. The modifications of the standard WJ-EARSM proposed in Paper 3 improved both  $\overline{u^2}$  and K.

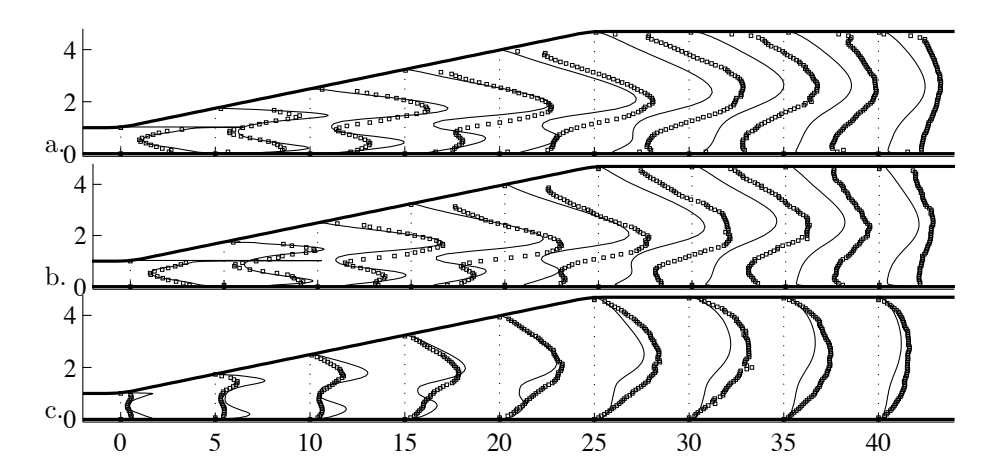


FIGURE 5.5. Experimental data ( $\square$ ) and WJ-EARSM (—) predictions for turbulence quantities for the 8.5° case: a) turbulence kinetic energy  $(500K/U_b^2)$ , b) variance of the streamwise velocity component  $500\overline{u^2}/U_b^2$ c) variance of the wall-normal (y-direction) velocity component  $(500\overline{v^2}/U_b^2)$ . Dotted line shows zero-level at each position.

# 5.3.3. Passive scalar modelling

The turbulent flow in the asymmetric diffuser, described in previous section, was also used in calculation of passive temperature transport. Different temperature boundary conditions were imposed at the walls and the turbulent transport of the passive temperature was studied. The heat flux vector was modelled using the algebraic scalar flux model (EASFM) with constant time scale ratio described in Paper 2. A comparison of a standard eddy-diffusivity model (EDM) and EASFM in prediction of the mean scalar  $\Theta$  is shown in figure 5.6 for both the 8.5° and 10° diffusers with a fixed difference  $\Delta\Theta$  between the upper and lower walls. From this it is clearly seen that the mean scalar filed predicted by the EDM is barely affected by the presence of a separation region along the inclined wall. The mean scalar field obtained from the use of EASFM shows a region of constant  $\Theta$  forming at the separation point and located at the dividing streamline in the wall-normal direction. The wall-normal extent of this region grows in the streamwise direction in the region of separated flow. Downstream of the reattachment point this feature slowly diminishes. The heat flux vector field, shown in figure 5.7, clearly shows the advantage of using a more advanced scalar flux model, whose component are not aligned with the mean scalar gradient. The EDM field in 5.7b is a simple transport from the wall with high  $\Theta$  to the wall with low  $\Theta$ , implying a dominant  $v\theta$  component. In the case of EASFM, the two flux components are large and of equal magnitude outside the separation region and with small contributions inside the separation region.

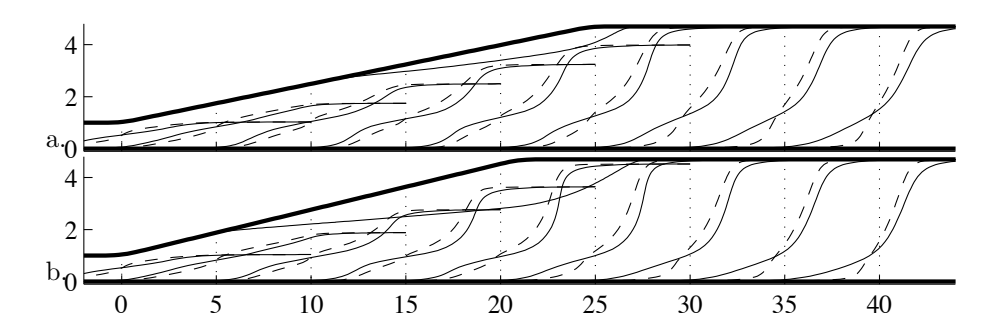


FIGURE 5.6. Comparison of temperature distribution (10 $\Theta$ ) between EASFM (—) and EDM (– –) for the diffuser at a) 8.5° and b) 10°.

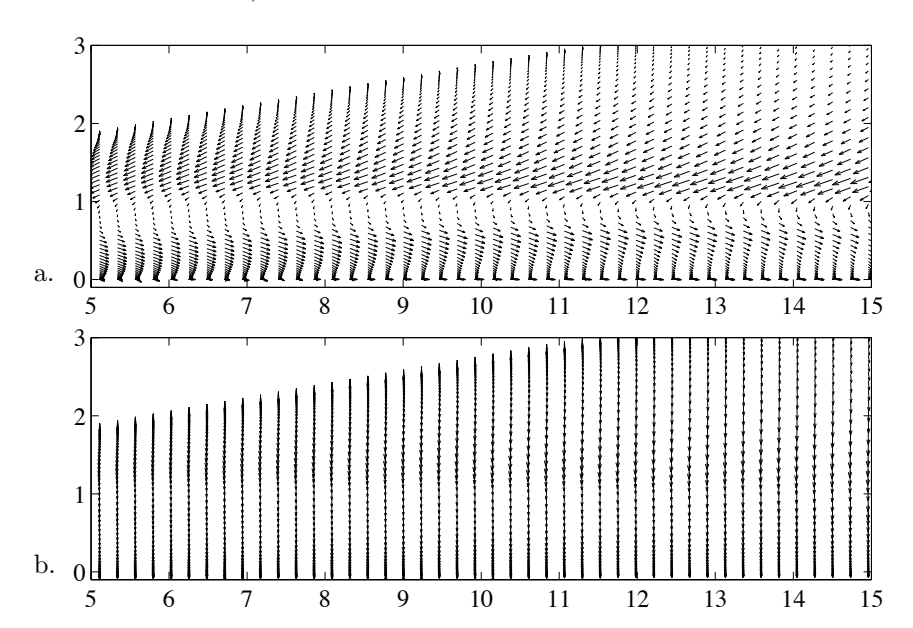


FIGURE 5.7. Scalar flux vector in part of the diffuser at  $10^{\circ}$  opening angle for a) EASFM and b) EDM. The axis are of equal scale for the sake of comparison.

## CHAPTER 6

# Conclusions

The framework of automated code generation has significantly increased the possibility to quickly and accurately implement several systems of equations that govern turbulent flow. The momentum equations have been solved using a fractional step method and the turbulence models comprise of differential Reynolds stress model and explicit algebraic Reynolds stress models based in the K- $\omega$  platform. Low-Reynolds number corrections have been included in each model where appropriate, and a decomposition of the  $\omega$ -equation has been validated. A differential equation has been derived and verified to obtain the closest wall-normal distance from any point in the computational domain, regardless of number of spatial dimensions or geometric complexity.

The decomposition of  $\omega$  has successfully been implemented in three widely used formulations of the transport equation for  $\omega$  and analysis show that it is compatible with most formulations today, independent of level of the modelling of the Reynolds stress anisotropy.

All models have been calibrated in fully developed plane channel flow and used in asymmetric diffuser flow to asses the ability to predict flow separation. Two inclination, or opening, angles have been used,  $8.5^{\circ}$  and  $10^{\circ}$ . The low-Re EARSM of Wallin & Johansson (2000) in combination with Wilcox (1993) low-Re K- $\omega$  platform does not predict the same extent of the separation region as observed in experiments at  $8.5^{\circ}$ . The agreement can be improved by modifying one of the model coefficients of the underlying pressure-strain rate model, yielding higher levels of turbulence kinetic energy downstream of the separation point. In the  $10^{\circ}$  case the wall-normal extent of the separated region shows good agreement with experimental data from Buice & Eaton (2000), while the location of the reattachment point is underestimated. This is also improved with the modified EARSMs. It was also found that the results obtained by the DRSM was rather consistent with the corresponding EARSM, indicating that the algebraic assumption can be used in this case.

The explicit algebraic scalar flux model derived by Wikström et al. (2000) has been used to model passive scalar transport in both fully developed turbulent channel flow and asymmetric diffuser flow. Compared to an eddy-diffusivity model, the advantages of this higher-order modelling for the scalar flux has been shown for separated flows for several types of boundary conditions.

## APPENDIX A

# Pressure-sensitive paint

One possible measurement technique to obtain the pressure distribution on a surface of complex geometry is the use of an optical/chemical approach involving pressure-sensitive paint (PSP). The first article on the use of pressure-sensitive paint in fluid flow was reported by Peterson & Fitzgerald (1980), where the method was used to as a qualitative surface visualization technique. Today the technique is used to obtain quantitative 2D pressure fields from an aero-dynamic surface and has attracted interest from both the research community and aircraft manufacturers since the early 90's. The main area of application is in wind-tunnel testing, but at least one system based on 35-mm film has been developed for in-flight measurements, see Abbitt et al. (1996).

The principle approach when using the PSP is to form a surface coating consisting of a luminescent dye in combination with a polymer primer. The paint is exposed by a narrow band light source, where the appropriate exposure wave length depending on the paint, ranging from 390 nm to 450 nm, while the luminescent particles in the paint excite a 'red-shifted' light (650–750 nm). The intensity of the excited light is dependent on the local surface pressure, hence the luminescence is quenched by the presence of oxygen. The light excited from the paint is registered by a CCD-camera and the image is processed to obtain a pressure map.

The pressure can be obtained either by registering the decay time, or life time, of the excited light when the exposing light is delivered during a short time, or by registering the intensity of the excited light integrated over a certain exposure time with a continuous light source. Life time measurements are recommended in transient or unsteady flow, where response times have been reported in the range from 3 ms (Hubner et al. (1997)) down to 10  $\mu$ s (Asai et al. (2001)). Davies et al. (1995) concluded that the response time to a stepchange in pressure is proportional to the square of the paint thickness, with a typical thickness of dye and primer less in the order of 20  $\mu$ m.

The luminescence process was described by Morris  $et\ al.\ (1993)$  as a mechanism where the molecules of the luminescent dye can lose the excess energy gained from the exposing light source by emitting a photon and return to the ground state. Non-homogenous paint thickness and uneven illumination can be compensated by comparing a 'wind on' image with an image at constant, often controlled, pressure. The relation between pressure p and intensity I is

defined by

$$\frac{p}{p_{\text{ref}}} = \sum_{i=0}^{n} c_i \left(\frac{I_{\text{ref}}}{I}\right)^i, \tag{A.1}$$

where subscript 'ref' denotes the reference image and  $c_i$  are calibration coefficients. In low-speed applications the variation in pressure is small and n=1 is sufficient, called the Stern-Volmer relation. The transonic flow described in Paper 6 included a large pressure gradient and n=4 was used instead.

The main advantage of using PSP is, as stated above, the possibility to obtain the pressure field of any aerodynamic surface, in contrast to the method of using a distribution of discrete pressure-taps. The process of determining where to put the taps and fitting them into the surface can be both complicated and time consuming. In the paper by McLachlan & Bell (1995) it was estimated that 30% of the cost of an aircraft wind tunnel model for determining surface loads originated from pressure tap manufacturing and installation. The PSP can applied to any surface, even at sharp corners, e.g. at the trailing edge of an airfoil.

The are, however, several drawbacks. In high speeds, deformation of the wind-tunnel model between wind-on and wind-off conditions make it difficult to obtain accurate predictions. In many cases the PSP exhibit temperature-sensitive characteristics, especially in low-speed flows. In Schanze et al. (1997), the main conclusion was that the temperature sensitivity is dependent on the diffusion time of oxygen trough the polymer binder. The use of dual life time paints have been proposed by e.g. Hradil et al. (2002), Zelow et al. (2003) and Gouterman et al. (2004) to remedy this problem.

With the development of more sensitive paints for low-speed applications, the automotive industry have shown increasing interest. Morris (1995) conducted PSP measurements on delta-wing shaped geometries down to Mach 0.5 (; 20 m/s). Measurements for automotive (Gouterman  $et\ al.\ (2004)$ ) and aeronautical (Engler  $et\ al.\ (2002)$ ) applications have been performed down to 25 m/s. The temperature dependence on the pressure measurements is very important in these flows and must be treated carefully, by e.g. dual lifetime as described by Gouterman.

In Paper 6, experiments in a 2D transonic nozzle has been carried out using PSP, pressure taps and thermocouples. Good agreement was achieved through the arc-shaped nozzle for pressure obtained with pressure taps along the centerline and PSP. The PSP data was transformed to Mach number using isentropic relations and a good agreement was also obtained when comparing with computational predictions.

# Acknowledgments

First of all I would like to thank my supervisor Professor Arne Johansson for all the support and inspiration that you have given me throughout the years. You have provided me with both an excellent working environment and all the technical resources I've needed. My future superiors will have a hard time living up to the standards you've set. The course of my project has not been a straight one, but you have helped and encouraged me to try new paths.

I would also like to thank Professor Gustav Amberg for his help as assisting supervisor, his never ending enthusiasm concerning the automated code generation procedure and his annoying ability to always be one step ahead of me in my train of thoughts.

Thanks are also extended to my second assisting supervisor, Dr. Stefan Wallin. His experience of Reynolds stress models and asymmetric diffuser flow have helped widening my field of view concerning the novelties of the models. It is too bad the collaboration has to end so soon.

Financial support from the Integral Vehicle Structures research school is gratefully acknowledged.

Of course, my room-mates at the department, Gustaf, Olof and Arnim have all supported me with fruitful discussions, sharing experiences and academic gossip over the endless cups of coffee. Gustaf, you deserve an extra remark for the inspiring attitude and surprises. I'll always cherish the SubRosa-meetings, the geek t-shirt and Christmas presents.

The turbulence group, with my room-mates and Olle, Björn, Geert and Linus, all contributing to a great working environment. Thanks you. I've also spent a lot of my time in the Lab, so I must not forget mentioning Fredrik, Kristian, Jens, Davide, Luca, Timmy, Thomas, Claes, Richard and many more who helped me keep in touch with the experimental part of fluid mechanics.

Also all the other doctoral students and teachers at the department, past and present, have contributed to a pleasant six years.

Bruce Carroll was my supervisor during my short stay at the University of Florida, the spring of 1999. Thanks are extended to you and your group for guiding me and letting me experience a piece of the sunshine state.

# 36 ACKNOWLEDGMENTS

I owe a great deal of gratitude to Tekn.Lic.Civ.Ing.pret.snob. Tomas Melin. We've shared most my eleven years at KTH and you've provided me with a lot of happy moments, fun stories and genuine support. Thank you.

To my parents, Lars and Fänta, to whom this thesis is dedicated, I extend my deepest gratitude. For a lifetime of support and sacrifice, how can I ever repay you?

For count-less hours of baby-sitting during the last period of non-stop thesis-writing I thank Jeanette and Curre. I wouldn't have finished in time without you.

Thanks are extended to my family, Madeleine and Felicia, for being the loves of my life, putting up with all the late hours and support when I didn't believe in myself.

# **Bibliography**

- Abbitt, J. D., Fuentes, C. A. & Carroll, B. F. 1996 Film-based pressure-sensitive-paint measurements. *Optics Letters* **21** (22), 1797–1799.
- ABE, K., KONDOH, T. & NAGANO, Y. 1996 A two-equation heat transfer model reflecting second-moment closures for wall and free turbulent flows. *Int. J. Heat and Fluid Flow* 17, 228–237.
- Amberg, G., Törnhardt, R. & Winkler, C. 1999 Finite element simulations using symbolic computing. *Mathematics and Computers in Simulation* 44, 275–274.
- APSLEY, D. D. & LESCHZINER, M. A. 2000 Advanced turbulence modelling of separated flow in a diffuser. Flow, Turbulence and Combustion 63 (1–4), 81–112.
- ASAI, K., NAKAKITA, K., KAMEDA, M. & K.TEDUKA 2001 Recent topics in fast-responding pressure-sensitive paint technology at National Aerospace Laboratory. In *ICIASF 2001 Record*, 19th International Congress on Instrumentation in Aerospace Simulation Facilities, pp. 25–36.
- Bredberg, J., Peng, S.-H. & Davidson, L. 2002 An improved  $k-\omega$  turbulence model applied to recirculating flow. *Int. J. Heat and Fluid Flow* **23**, 731–743.
- Buice, C. U. & Eaton, J. K. 2000 Experimental investigation of flow through an asymmetric plane diffuser. *J. Fluids Eng.* **122**, 433 435.
- Craft, T. J. 1998 Developments in a low-Reynolds number second-moment closure and its application to separating and reattaching flows. *Int. J. Heat Fluid Flow* 19, 541–548.
- Craft, T. J. & Launder, B. E. 1996 A Reynolds stress closure designed for complex geometries. *Int. J. Heat Fluid Flow* 17, 245–254.
- Daly, B. J. & Harlow, F. H. 1970 Transport equations in turbulence. Int. Phys. Fluids  ${\bf 13},\,2634-2649.$
- Davies, A. G., Bedwell, D., Dunleavy, M. & Brownjohn, N. 1995 Pressure sensitive paint limitations and solutions. In 7th International Symposium on Flow Visualization, pp. 11–21.
- Durbin, P. A. 1993 Application of a near-wall turbulence model to boundary layers and heat transfer. *Int. J. Heat Fluid Flow* 14, 316–323.
- DURBIN, P. A. 1995 Separated Flow Computations with the  $k-\varepsilon-v^2$  model. AIAA Journal 33, 659–664.
- ENGLER, R. H., MÉRIENNE, M.-C., KLEIN, C. & SANT, Y. L. 2002 Application of PSP in low speed flows. *Aerospace Science and Technology* **6**, 313–322.

- Gatski, T. B. & Speziale, C. G. 1993 On explicit algebraic stress models for complex turbulent flows. *J. Fluid Mech.* **254**, 59–78.
- GOUTERMAN, M., CALLIS, J., DALTON, L., KHALIL, G., MÉBARKI, Y., COOPER, K. R. & GRENIER, M. 2004 Dual luminophore pressure-sensitive paint: III. Application to automotive model testing. *Meas. Sci. Technol.* **15**, 1986–1994.
- Gresho, P. M. & Sani, R. L. 1998 Incompressible Flow and the Finite Element Method. John Whiley and Sons.
- Guermond, J. L. & Quartapelle, L. 1997 Calculation of incompressible vicous flow by an unconditionally stable projection fem. *J. Computational Physics* **132** (CP965587), 12–33.
- Hanjalić, K., Popovac, M. & Hadžiabdić, M. 2004 A robust near-wall elliptic-relaxation eddy-viscosity turbulence model for CFD. *Int. J. Heat Fluid Flow* **25** (6), 1047–1051.
- Hellsten, A. 2004 New advanced  $k-\omega$  turbulence model for high-lift aerodynamics. In 42nd AIAA Aerospace Sciences Meeting and Exhibit, pp. 1–18. Reno, NV, USA.
- Hellsten, A. & Rautaheimo, P., ed. 1999 8th ERCOFTAC/IAHR/COST Workshop on Refined Turbulence Modelling. Helsinki University of Technology, Finland.
- HÖGSTRÖM, C.-G., WALLIN, S. & JOHANSSON, A. V. 2001 Passive scalar flux modelling for CFD. In 2nd International Symposium on Turbulence and Shear Flow Phenomena, , vol. II, pp. 383–388. Stockholm, Sweden.
- Hradil, J., Davies, C., Mongey, K., McDonagh, C. & MacCraith, B. D. 2002 Temperature-corrected pressure-sensitive paint measurements using a single camera and a dual-lifetime approach. *Meas. Sci. Technol.* **13**, 1552–1557.
- Hubner, J. P., Carroll, B. F., Schanze, K. S. & Ji, H. F. 1997 Techniques for using pressure-sensitive paint in shock tunnel facilities. In ICIASF'97 Record. International Congress on Instrumentation in Aerospace Simulation Facilities, pp. 30–39.
- IACCARINO, G. 2000 Prediction of the turbulent flow in a diffuser with commercial CFD codes. *Tech. Rep.*. Center for Turbulence Research.
- Johansson, A. V. 2002 Engineering turbulence models and their development, with emphasis on explicit algebraic Reynolds stress models, pp. 1–30. Springer.
- Kaltenbach, H. J., Fatica, M., Mittal, R., Lund, T. S. & Moin, P. 1999 Study of flow in a planar asymmetric diffuser using large-eddy simulation. J. Fluid Mech. 390, 151–185.
- KAWAMURA, H., ABE, H. & MATSUO, Y. 1999 DNS of turbulent heat transfer in channel flow with respect to Reynolds and pandtl number effects. *Int. J. Heat and Fluid Flow* 19, 482–491.
- Kim, J. & Moin, P. 1989 Transport of Passive Scalars in a Turbulent Channel Flow, pp. 85–96. Springer.
- LAUNDER, B. E., REECE, G. J. & RODI, W. 1975 Progress in the development of a Reynolds stress turbulence closure. *J. Fluid Mech.* **210**, 537–566.
- McLachlan, B. G. & Bell, J. H. 1995 Pressure-sensitive paint in aerodynamic testing. *Experimental Thermal and Fluid Science* **10**, 470–485.
- Menter, F. R. 1994 Two-equation eddy viscosity turbulence models for engineering applications. *AIAA Journal* **32** (8), 1598–1605.

- Morris, M., Donovan, J., Kegleman, J., Schwab, S. D., Levy, R. & Crites, R. C. 1993 Aerodymamic applications of pressure sensitive paint. *AIAA Journal* 31 (3).
- MORRIS, M. J. 1995 Use of pressure-sensitive paints in low-speed flows. In 16th Int Congress Instrumentation in Aerospace Simulation Facilities (ICIASF), IEEE. Wright-Patterson AFB, Dayton OH.
- NAGANO, Y. & SHIMADA, M. 1996 Developement of a two-equation heat transfer model based in direct simulations of turbulent flows with different prandtl numbers. *Phys. Fluids* 8 (12), 3379–3402.
- Obi, S., Aoki, K. & Masuda, S. 1993a Experimental and computational study of separating flow in an asymmetric planar diffuser. In 9th Symposium on Turbulent Shear Flows, , vol. 305, pp. 1–4. Kyoto, Japan.
- Obi, S., Ohizumi, K., Aoki, K. & Masuda, S. 1993b Turbulent separation control in a plane asymmetric diffuser by periodic perturbation, pp. 633–642. Elsevier Science Publishers B.V.
- Peng, S.-H., Davidson, L. & Holmberg, S. 1997 A modified low-Reynolds-number  $k\text{-}\omega$  model for recirculation flows. J. Fluids Eng. 119, 867–875.
- Peterson, J. I. & Fitzgerald, V. F. 1980 New technique of surface flow visualization based in oxygen quenching of fluorescence. *Review of Scientific Instruments* **51** (5), 670–671.
- Piquet, J. 1999 Turbulent flows. Springer-Verlag.
- ROKNI, M. & SUNDÉN, B. 2003 Investigation of a two-equation turbulent heat transfer model applied to ducts. *Trans. ASME, J. Heat Transfer* **125**, 194–200.
- Schanze, K. S., Carroll, B. F., Korotkevitch, S. & Morris, M. J. 1997 Temperature dependence of pressure sensitive paints. *AIAA Journal* **35** (2), 206–310.
- Sethian, J. A. 1996 Level Set Methods and Fast Marching Methods. Cambridge University Press.
- SHIMA, N. 1988 A Reynolds stress model for near wall and low-Reynolds number regions. J. Fluids Eng. 110, 38–44.
- SJÖGREN, J. 1997 Development and validation of turbulence models through experiment and computation. Doctoral thesis. Dept. of Mechanics, KTH, Sweden.
- Speziale, C. G., Sarkar, S. & Gatski, T. B. 1991 Modelling the pressure-strain correlation of turbulence: an invariant dynamical systems approach. *J. Fluid Mech.* 227, 245–272.
- Tennekes, H. & Lumley, J. L. 1972 A First Course in Turbulence. The MIT Press.
- Wallin, S. & Johansson, A. V. 2000 An explicit algebraic Reynolds stress model for incompressible and compressible turbulent flows. *J. Fluid Mech.* **403**, 89–132.
- Wikström, P. M., Wallin, S. & Johansson, A. V. 2000 Derivation and investigation of a new explicit algebraic model for the passive scalar flux. *Physics of Fluids* **12** (3), 688–702.
- WILCOX, D. C. 1993 Turbulence modeling for CFD. DCW Industries Inc.
- Zelow, B., Khalil, G. E., Phelan, G., Carlson, B., Gouterman, M., Callis, J. B. & Dalton, L. R. 2003 Dual luminophore pressure sensitive paint II. lifetime based measurement of pressure and temperature. *Sensors and Actuators B* **96**, 304–314.